Title

Tailoring the structure and electrochemical performance of sodium titanate anodes by post-synthesis heating

Journal

Journal of Materials Chemistry A, 10(47)

ISSN

2050-7488

Authors

Yin, Wei
Barim, Gözde
Peng, Xinxing
et al.

Publication Date

2022-12-06

DOI

10.1039/d2ta07403f

Tailoring the Structure and Electrochemical Performance of Sodium Titanate Anodes by Post-synthesis Heating

Wei Yin,[a] Gözde Barim,[a] Xinxing Peng,[b, c] Elyse A. Kedzie,[a, d] Mary C. Scott,[b, c] Bryan D. McCloskey,[a, d] and Marca M. Doeff [a, *]

[a] Energy Storage & Distributed Resources Division, Lawrence Berkeley National Laboratory, Berkeley, CA 94720, USA.
[b] Department of Materials Science and Engineering, University of California Berkeley, Berkeley, CA 94720, USA
[c] National Center for Electron Microscopy, Molecular Foundry, Lawrence Berkeley National Laboratory, Berkeley, CA 94720, USA
[d] Department of Chemical and Biomolecular Engineering, University of California Berkeley, Berkeley, CA, 94720, USA
* E-mail: mmdoeff@lbl.gov

Abstract

Sodium titanate anodes synthesized *via* "chimie-douce" methods generally require a post-synthesis dehydration step. Their crystal structures are sensitive to the heating conditions such as temperature, resulting in distinct sodium storage performance. Herein, using *in situ* and *ex situ* high-temperature X-ray diffraction, we studied in detail the structural changes of $Na_{0.74}Ti_{1.815}\bullet_{0.185}O_4\bullet 1.27H_2O$ (NTO) under various heating conditions. Electrochemical characterization revealed that NTOs heated at lower temperatures with layered structures deliver larger capacities than those heated at high temperatures with tunnel structures. Moderate temperature heat treatment greatly improves the capacity retention of NTO, especially stabilizing the high voltage processes that are major contributors to the capacity fading, because of the modified crystal structure and surface chemistry. Our findings suggest that post-synthesis heating is a simple and effective strategy to tailor the crystal structure, surface chemistry, and electrochemical properties of sodium titanate anodes.

Introduction

Lithium (Li)-ion batteries have made today's mobile society possible; however, soaring energy demands raise concerns about the sustainability of lithium sources and the transition metals used for manufacturing electrode materials.[1] With the intrinsic advantage of resource abundance, sodium (Na)-ion batteries are expected to relieve pressure on Li supplies. Furthermore, sodium metal oxide cathodes can be made from naturally abundant metals (*e.g.*, iron, manganese, and titanium), making Na-ion batteries a sustainable and cost-effective complement to Li-ion batteries in application scenarios such as stationary energy storage and short-range, low-cost electric vehicles.[2-4] After decades of academic and industry research, the Faradion Na-ion chemistry can now exceed the energy densities of $LiFePO_4$//graphite Li-ion batteries (Faradion Na-ion: ~ 160 Wh kg^{-1} in 32 Ah pouch cells, Pylontech $LiFePO_4$//graphite Li-ion: ~ 145 Wh kg^{-1} in 25 Ah pouch cells), with similar rate performance, improved safety and lower cost.[5] Nevertheless, advanced anode and cathode materials are needed to further push the specific energies of Na-ion batteries towards 200 Wh kg^{-1}.[2]

Sodium titanates are among the most promising anode materials for Na-ion batteries, due to their low cost, possibility of high tap density, and relatively higher operation voltage compared to the commonly used hard carbons, which can prevent metallic sodium plating.[5] However, these oxides have a finite number of sites for ion insertion, which limits the Na^+ storage capacity, and thereby the achievable energy densities. The sluggish Na^+ (de)intercalation kinetics and poor electronic conductivity are other impediments to the practical capacity. The presence of mobile cations (*e.g.*, Li^+) instead of less mobile ones (*e.g.*, Mg^{2+}) in the metal oxide layers has previously been shown to provide additional diffusional pathways for Na^+ and improves the practical capacities.[6] This observation motivated us to design and synthesize lepidocrocite-structured titanates with titanium vacancies in the transition metal layers, on the assumption that these vacancies will have similar beneficial effects as mobile cations.[7] The non-stoichiometric sodium titanate $Na_{0.74}Ti_{1.815}\bullet_{0.185}O_4\bullet 1.27H_2O$ indeed shows a higher capacity of 229 mAh g^{-1}, however, its cycling stability still needs to be improved.[7] Titanates synthesized *via* "chimie-douce" methods generally require a post-synthesis dehydration step and their crystal structures are highly dependent on the dehydration conditions such as temperature, time, atmosphere, initial water content *etc.*, leading to distinct electrochemical properties when used as anode materials.[8-11] Identifying the correlation between heating-induced structural changes and electrochemical properties is relevant for the performance optimization of titanate anodes. For instance, Katogi *et al.* reported that, upon heating to 350 ˚C, the hydrous P-type (space group *Pmmm*) $Na_{0.9}[Ti_{1.7}Li_{0.3}]O_4\bullet nH_2O$ transforms into the anhydrous C-type (space group *Cmcm*) phase as a result of gradual removal of the interlayer water.[11] The C-type $Na_{0.9}[Ti_{1.7}Li_{0.3}]O_4$ electrode shows more pronounced plateau features and higher initial Coulombic efficiency although no significant difference was found in the cycling performance.[11]

Herein, we employed a post-synthesis heating strategy to tune the crystal structure and thereby to optimize the electrochemical properties of lepidocrocite-type sodium titanate anode $Na_{0.74}Ti_{1.815}\bullet_{0.185}O_4\bullet 1.27H_2O$ (NTO). *In situ* and *ex situ* high temperature X-ray diffraction (XRD) together with *ex situ* Raman spectroscopy were first employed to investigate the structural changes of NTO upon heating from room temperature to 800 ˚C. Coupling structural studies and electrochemical characterization, we uncovered the correlations between heating-induced structural changes and their sodium storage behavior. Furthermore, we demonstrated that the optimized performance could be achieved by heat treatment at moderate temperature (500 ˚C). In contrast to the 60 ˚C-heated material which retain only 64.8 % of its reversible capacity (228.1 mAh g^{-1}) in the 50th cycle at a current rate of 8 mA g^{-1}, the 500 ˚C-heated material shows stable cycling with 94.3 % of its reversible capacity (184 mAh g^{-1}) in the 50th cycle at current rate of 8 mA g^{-1} and 80.1 % of its reversible capacities (150.8 mAh g^{-1}) in the 743th cycle at elevated current rate of 200 mA g^{-1}. *Ex situ*

synchrotron XRD and X-ray absorption spectroscopy were also employed to unravel respectively the cycling-induced structural evolutions and the reaction mechanisms of 60 ˚C- and 500 ˚C-heated NTOs.

Results and Discussion

Lepidocrocite (γ-FeOOH)-type sodium titanate (nominal composition of $Na_{0.74}Ti_{1.815}\bullet_{0.185}O_4 \cdot 1.27H_2O$, termed NTO hereafter) powders were prepared by high-temperature reaction from Cs_2CO_3 and anatase precursors followed by aqueous Cs^+/Na^+ ion-exchange, as detailed elsewhere.[7] The body centered orthorhombic *Immm* structure of NTO was confirmed by X-ray diffraction (XRD)[7]. To study its heating-induced structural changes, *in situ* high-temperature synchrotron XRD measurements were conducted under air from room temperature to 775 ˚C (Figures 1a & 1b). Le Bail analyses of the XRD patterns suggest that the initial layered *Immm* structure was largely maintained during heating from room temperature to 150 ˚C (Figures 1c & S1). A right-shift of the (020) diffraction line located at 2θ = 9.86˚ and a decrease in intensity of the (040) reflection located at 2θ = 19.8˚ are observed, indicating shrinkage of the interlayer distance caused by dehydration. Upon further elevating the temperature, new diffraction peaks appear at 2θ = 12.1˚, 29.8˚, 32.5˚, and 39.0˚ at the expense of the parent ones, indicating the formation of a new layered phase at 200 ˚C. A transition from the hydrous *Pmmm* phase to the anhydrous *Cmcm* phase due to heating-induced lateral gliding was reported for other lepidocrocite-like titanates such as $Na_x[Ti_{2-x/3}Li_{x/3}]O_4 \cdot nH_2O$,[10, 11] so we performed a structureless Le Bail fitting on the pattern collected at 200 ˚C using the *Cmcm* space group. The calculated pattern agrees well with the observed one with sufficiently small R-values (Figure 1d). The interlayer Na^+ is located within a rectangular prism coordinating with eight oxygen atoms in the *Immm* structure, while it is surrounded by six oxygen atoms in a trigonal prism in the *Cmcm* structure (Figures 1c & 1d). The refined unit cell parameters of the pristine and heated materials are compared in Table 1. The much smaller interlayer spacing of the 200 ˚C-heated phase (d_{020} = b/2 = 7.28 Å) compared to the room temperature phase (8.968 Å) indicates the removal of interlayer water. When the sample was further heated to higher temperatures, the (020) reflection gradually lost its intensity, and broad shoulders appear at both the higher- and lower angle side. Additionally, multiple new broad peaks began to develop in the 2θ range of 28 ~ 35˚ and 40 ~ 45˚. These broad peaks merge, evolve, and become sharper as the temperature increases to the end of

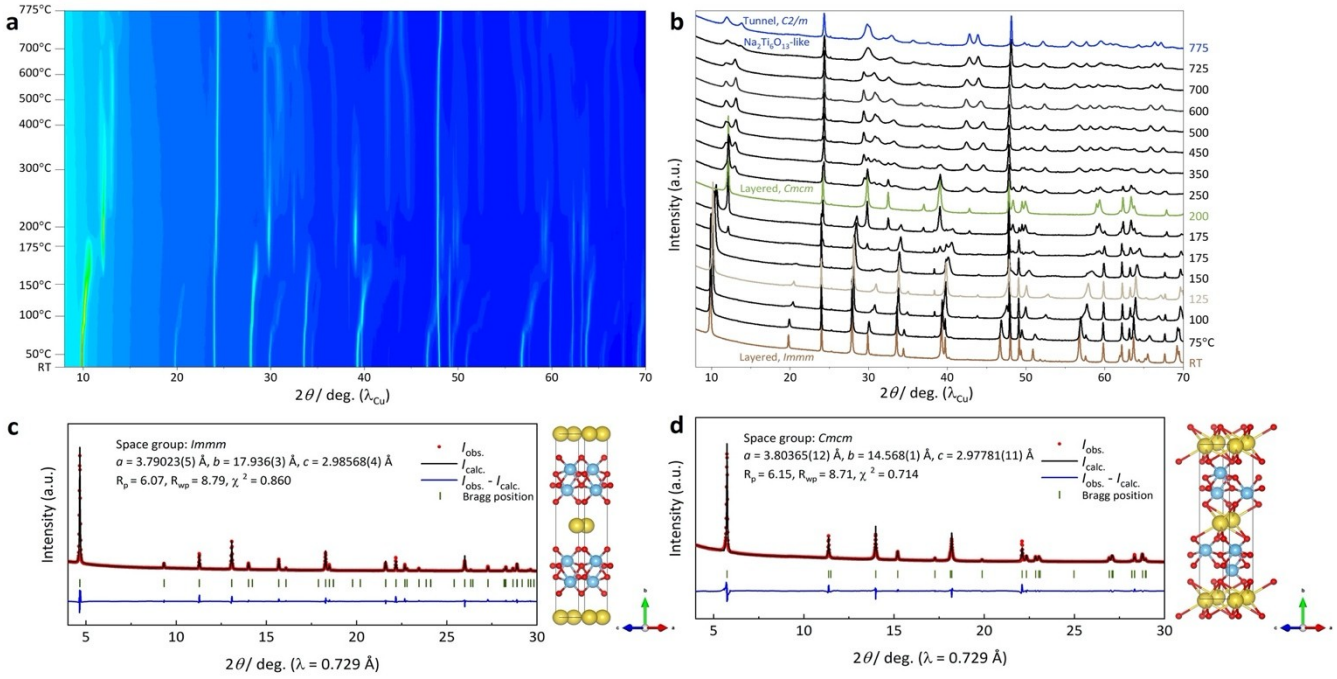

heating at 775 ˚C. The disappearance of

Figure 1. (a) Two-dimensional contour plot and (b) selected *in situ* high-temperature synchrotron XRD patterns of NTO collected from room temperature to 775 ˚C during the heating process in air. Note that the *x*-axes have been converted to 2θ CuKα values in (a) and (b). Le Bail fitting of XRD patterns collected at (c) room temperature using the *Immm* space group and (d) 200 °C using the *Cmcm* space group. The right side of panels (c) and (d) show the crystal structures of NTOs heated at (c) room temperature and (d) 200 °C visualized with VESTA. Gold spheres represent Na atoms and blue spheres represent Ti in octahedral sites.

the (020) peak and growth of new peaks clearly indicate that the layered *Cmcm* structure undergoes successive phase transitions. The resulting diffraction pattern at 775˚C is like that of $Na_2Ti_6O_{13}$, although the relative intensities of (200) and ($20\overline{1}1$) peaks (2θ = 11.8˚ and 13.9˚) compared to the (110) peak (2θ = 24.4˚) differ. Le Bail fitting of the pattern using the space group of $Na_2Ti_6O_{13}$ (*C2/m*) gave a reasonably good fit of the peak positions (Figure S1d). Note that the parent NTO has a higher Na:Ti ratio (0.41) than that of $Na_2Ti_6O_{13}$ (0.33), suggesting possible loss of interlayer Na^+ due to high-temperature heating. To maintain the charge neutrality caused by Na^+ loss, the formation of oxygen vacancies could also be expected, as previously discussed in other systems.[12, 13]

Table 1. Structural parameters of NTOs heated at various temperatures during the *in situ* high-temperature synchrotron XRD experiments.

Temperature (˚C)	Space group	a (Å)	b (Å)	c (Å)	β (˚)	R_p	R_{wp}	χ^2
Room temperature	I*mmm*	3.79023(5)	17.936(3)	2.98568(4)	90	6.07	8.79	0.86
100	I*mmm*	3.79758(11)	17.4395(11)	2.98114(10)	90	5.44	9.29	1.26
125	I*mmm*	3.80007(8)	17.331(1)	2.98163(7)	90	6.17	9.14	0.964
150	I*mmm*	3.80208(13)	17.0748(13)	2.98406(12)	90	6.11	10.5	1.62
200	*Cmcm*	3.80255(7)	14.5614(5)	2.97737(6)	90	4.65	8.36	1.00

Broadening of the diffraction peaks, most likely due to the structural disorder, *e.g.*, the positions of sodium ions inside the crystalline lattice, makes the profile fitting of XRD patterns collected at moderate and high temperatures difficult. Therefore, Raman spectroscopy was performed on NTOs heated *ex-situ* to gain additional structural information. In previous works on other sodium titanates, the Raman bands below 400 cm^{-1} and between 600 and 800 cm^{-1} have been attributed to Na–O bond vibrations and Ti–O stretching vibrations in edge- and corner-shared TiO_6 octahedra, respectively. Bands at higher frequencies (800 ~ 950 cm^{-1}) have been assigned to short Ti–O bonds of low coordination.[9, 14] As shown in Figure 2a, similar Raman spectra were obtained for the samples heated at 60 ˚C and 100 ˚C, showing Raman-active modes expected from the lepidocrocite structure of NTO.[7, 15] As the heating temperature continues to increase, the broad band at 796 cm^{-1} that was assigned to Ti–O–H vibrations became weak and finally disappeared, as a result of loss of OH– between TiO_6 layers caused by dehydration.[16] In addition, new bands grew in the ranges of 153 ~ 247 cm^{-1} and 325 ~ 410 cm^{-1}, along with the bands located at 659 and 705 cm^{-1} gradually merged into a single band. Raman spectra of the samples heated at 700 ˚C and 800 ˚C show similar characteristic bands as $Na_2Ti_6O_{13}$,[17, 18] providing additional evidence for their structural similarity. The Raman band at 871 cm^{-1} corresponds to the vibrations of the shortest Ti-O bonds in the tunnel structure of $Na_2Ti_6O_{13}$. Raman bands at 658 and 680 cm^{-1}, and 744 cm^{-1} are characteristic of the Ti-O-Ti stretch in the edge- and corner shared TiO_6 octahedra, respectively.[14] Although bands were observed at similar positions of 167, 194, 223, 392, and 411 cm^{-1} in the spectra of the 500 ˚C- and 600 ˚C-heated materials as in the spectrum of $Na_2Ti_6O_{13}$, their overall spectra are clearly different from $Na_2Ti_6O_{13}$. We speculate that the 500 ˚C- and 600 ˚C-heated materials could be intermediate phases with either pseudo-tunnel or layered/tunnel intergrown structures. Altogether, *in situ* high-temperature synchrotron XRD and *ex situ* Raman results demonstrated that the layered hydrous *Immm* structure of NTO first converts to a layered anhydrous *Cmcm* structure at 200 ˚C, and eventually transforms to a $Na_2Ti_6O_{13}$-like tunnel structure (space group *C2/m*) at high temperatures of 700 ˚C and above. Schematic illustrations of these structures are provided in Figure S2.

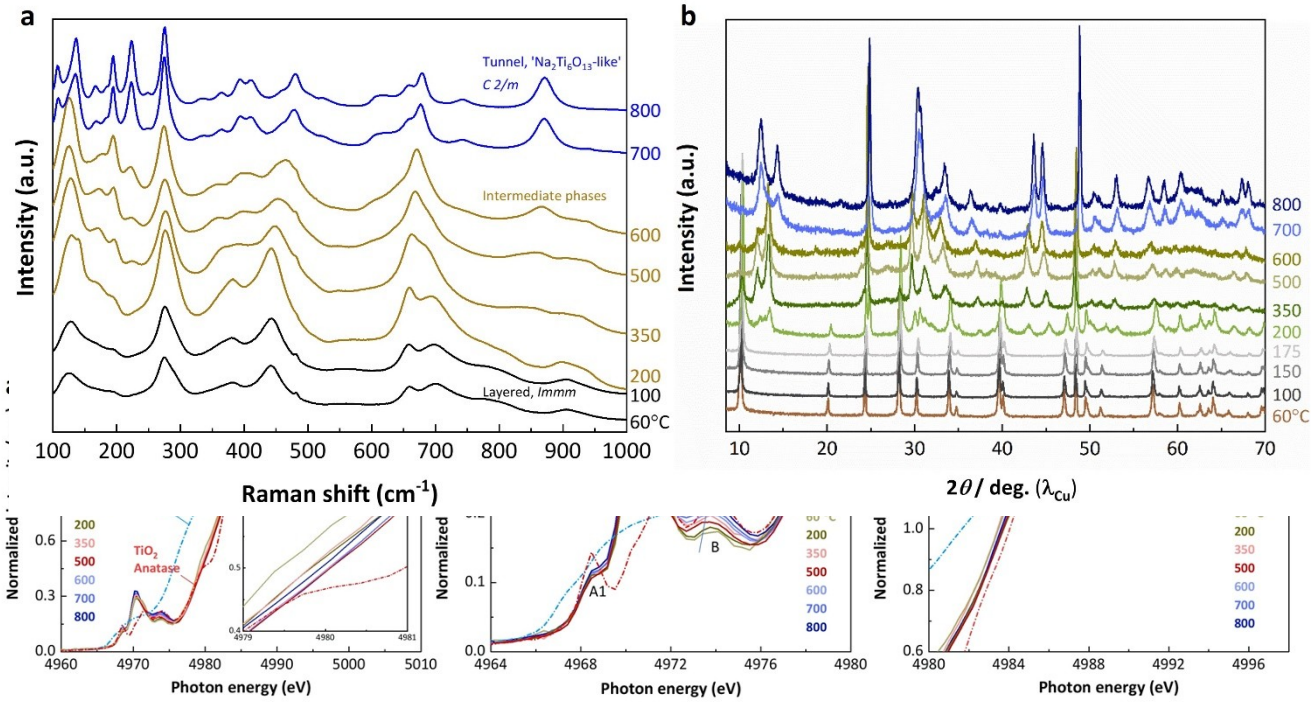

Figure 2. (a) Raman spectra and (b) laboratory XRD patterns of NTOs heated *ex situ* in air at temperatures ranging from 60 °C to 800 °C.

Ex situ XRD measurements were further employed to provide additional information about the heating-induced structural transitions of NTO (Figure 2b). Although a similar trend of structural transitions was observed during *ex situ* and *in situ* heating at temperatures greater than 350 ˚C, obvious differences appeared in the low-temperature range. Upon *ex situ* heating from 60 to 175 ˚C, the XRD patterns were nearly unchanged with a minor right-shift of the (020) diffraction line. In stark contrast to the *in situ* heating experiment, a mixture of the parent layered orthorhombic *Immm* phase and the intermediate phase was obtained after *ex situ* heating at 200 ˚C. This could be explained by differences in the heating time and/or temperature between *in situ* and *ex situ* heating, as well as the hygroscopic nature of NTO which causes the anhydrous phase to take up water and convert back to the hydrous phase in a short time frame that is beyond the detection limit of XRD. Since the electrodes for cell testing need to be pre-dried under vacuum to remove the water used for electrode preparation, we also evaluated the structures after low-temperature vacuum drying. The anhydrous layered *Cmcm* structure was obtained even after vacuum drying at 60 ˚C (Figure S3a). A mixture of the layered *Immm* phase and the intermediate phase was obtained after vacuum drying at 100 ˚C, which is similar to the phase obtained after *ex situ* heating under air at 200 ˚C (Figure S3b). Overall, these results demonstrated that the thermal behavior of NTO, especially at lower temperatures, is sensitive to the heating conditions, *i.e.*, heating protocol (*in situ* or *ex situ*) and atmosphere (air or vacuum).

Figure 3. (a) Ti K-edge X-ray absorption near-edge structure (XANES) spectra of NTOs heated in air at various temperatures. The inset in (a) shows the magnified view of the edge region. (b) and (c) show the zoom-in of the pre-edge peaks and the peaks near the absorption edge, respectively.

Next, to investigate the possible change of Ti oxidation state induced by heating, we measured Ti K-edge X-ray absorption near-edge structure (XANES) spectra of NTOs heated *ex situ* under air at various temperatures (Figure 3a). The absorption edges of XANES spectra of all the samples heated above 60 ˚C are close to the edge position of the anatase TiO_2 reference, indicating that Ti is primarily in the tetravalent state. The edge position of the 60 ˚C air-dried sample is at a slightly lower energy than Ti^{4+}, while NTO dried at the same temperature under vacuum shows a higher edge position close to Ti^{4+} (Figure S4). This suggests that the lower Ti K-edge position for the former is due to Ti atoms that are coordinated with hydroxyl groups. This is in line with the observation that the edge position gradually shifted to higher energy as the heating temperature increases (inset in Figure 3a). The removal of physiosorbed water by heating to higher temperature was also confirmed by *ex situ* Fourier transform infrared spectroscopy (FTIR) in attenuated total reflectance (ATR) mode (Figure S5). Further elevating the heating temperature to 800 ˚C resulted in edge shifting slightly towards lower energy, implying some thermally induced Ti^{4+} reduction (inset in Figure 3a). All the investigated NTO materials show similar pre-edge features consisting of four peaks designated A1, A2, A3 and B in Figure 3b. The pre-edge multiple peaks can be assigned to forbidden transitions from the core 1*s* level to unoccupied 3*d* state of Ti^{4+}, and their peak intensity is shown to be strongly dependent on the degree of distortion of the TiO_6 octahedron.[19] As shown in Figure 3b, the pre-edge peak intensity increases with higher heating temperature, implying more distortion of TiO_6 octahedra. Another noticeable difference is observed in the white line region. NTO heated at temperatures of 350 ˚C and above show two distinct white line peaks marked C1 and C2, whereas the 60 ˚C-heated NTO does not exhibit an apparent C1 peak (Figure 3c). The white line region of the Ti K-edge XANES spectra arises from dipole-allowed transitions from the core 1 *s* to unoccupied 4*p* states. The intensity of the C1 peak was proposed to be related to the edge-sharing octahedral width in a previous study.[20] It was shown that stepped titanates of $H_2Ti_3O_7$, $H_2Ti_4O_9{\bullet}1.2H_2O$, and $H_2Ti_5O_{11}{\bullet}3H_2O$ exhibit both C1 and C2 excitation peaks with the intensity of the C1 peak gradually decreasing in a sequence from $H_2Ti_3O_7$ (step size: 3), $H_2Ti_4O_9{\bullet}1.2H_2O$ (step size: 4), to $H_2Ti_5O_{11}{\bullet}3H_2O$ (step size: 5), whereas the lepidocrocite-type titanate $H_{0.7}Ti_{1.825}{\bullet}_{0.175}O_{4.0}{\bullet}H_2O$ in which the step size is one does not show an apparent C1 peak. Ti L-edge XANES spectra were also collected to provide information about the changes of local environment after *ex situ* heating. As shown in Figure S6, Ti L-edge spectra of all

the studied NTOs in total electron-yield (TEY) and fluorescence-yield (FY) modes show similar spectral features of two groups of peaks arising from the spin-orbit splitting of Ti 2*p* core level into $2p_{3/2}$ (L_3-edge) and Ti $2p_{1/2}$ levels (L_2-edge). These levels are further split by the strong ligand

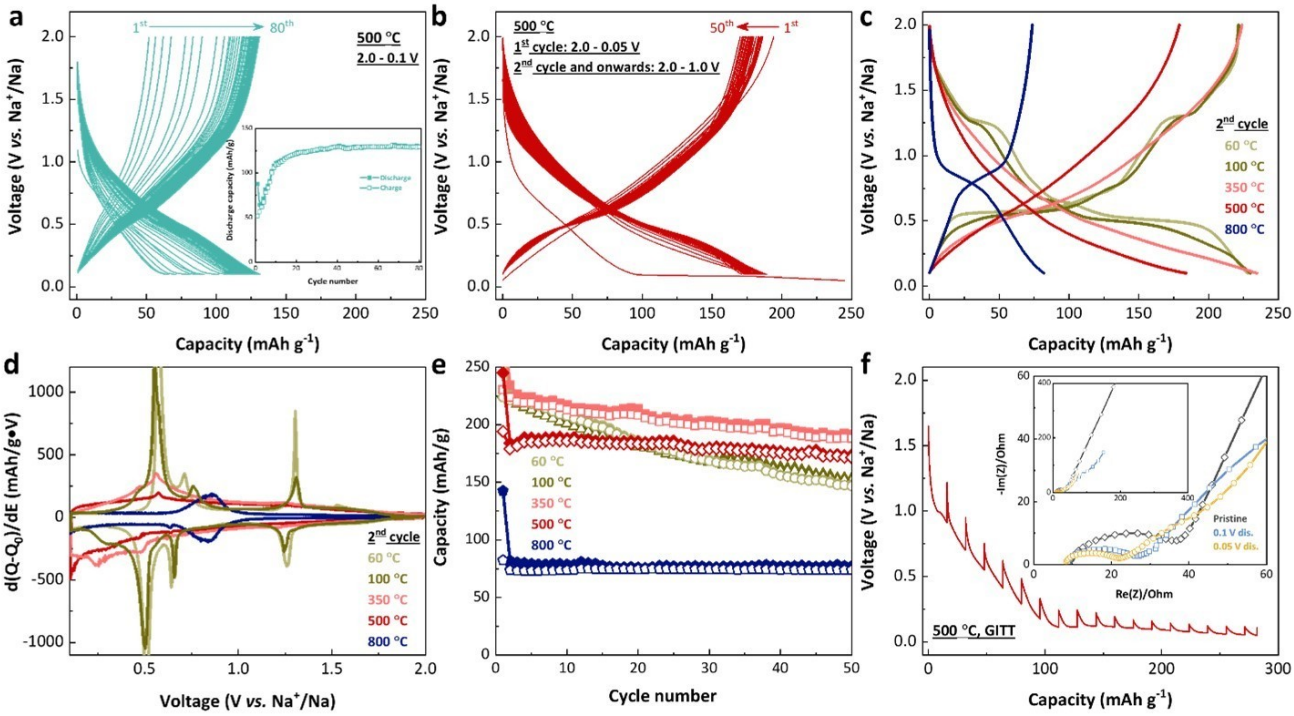

field arising from the surrounding oxygen atoms into two sublevels with t_{2g} and e_g symmetry. The e_g band is known to be highly sensitive to the local environment because the Ti e_g orbitals point directly towards the 2*p* orbitals of the surrounding O atoms.[21] The most prominent difference among the spectra of NTOs is the energy splitting of the fine structure in the L_3-e_g band. The L_3-e_g peak splitting observed in NTOs heated at lower temperatures of 60 and 200 °C was absent in NTOs heated to temperatures of 500 °C and above. The origin of L_3-e_g splitting is still under debate in the literature; proposed explanations include TiO_6 octahedra connectivity or local distortion of individual octahedra.[22, 23] Overall, the variations in the white line characteristics of C1 and C2 observed in Ti K-edge XANES spectra and the difference in the L_3-e_g peak splitting of Ti L-edge XANES spectra suggest a thermally induced conversion of lepidocrocite-type layered to stepped titanate, which agrees well with the structural insights provided by the high-temperature XRD experiments.

Figure 4. Galvanostatic discharge-charge voltage profiles of sodium half cells containing 500 °C-heated NTO cycled between 0.1 and 2.0 V *vs.* Na^+/Na (a) without and (b) with an initial 'activation' cycle between 0.05 and 2.0 V *vs.* Na^+/Na. The inset in (a) shows the discharge capacity as a function of cycle number. (c) The second cycle galvanostatic discharge-charge voltage profiles between 0.1 and 2.0 V *vs.* Na^+/Na of NTOs heated to the indicated temperatures (d) the corresponding *dQ*/*dV* plots, and (e) capacity retention over 50 cycles. For the initial cycle, a cycling voltage window of 0.1 - 2.0 V *vs.* Na^+/Na is used for 60 °C- and 100°C-heated NTOs, while 0.05 - 2.0 V *vs.* Na^+/Na is used for 350 °C-, 500 °C-, and 800 °C heated NTOs. (f) Galvanostatic intermittent titration technique (GITT) voltage profile of 500 °C-heated NTO, the inset shows the evolution of electrochemical impedance spectroscopy (EIS) spectra as a function of discharge potentials. All the cells were cycled at a current rate of 8 mA g^{-1} (0.008 mA cm^{-2}) using a sodium metal anode and a solution of 0.5 M $NaBPh_4$ in DEGDME as the electrolyte.

We then evaluated the electrochemical performance of NTOs heated under air at 60, 350, 500, and 800 °C. All the prepared electrodes were vacuum dried at 60 °C overnight before assembly into sodium half cells using an electrolyte of 0.5 M sodium tetraphenylborate ($NaBPh_4$) in diethylene glycol dimethyl ether (DEGDME). Electrodes made with 60 °C-heated NTO that were further vacuum dried at 100 °C were also included for comparison. As shown in Figure S7, when cycled in the voltage window of 0.1 - 2.0 V *vs.* Na^+/Na, the specific charge capacities obtained in the first cycle for NTOs heated at 350 (111.0 mAh g^{-1}) and 500 °C (51.7 mAh g^{-1}) were rather low compared to 60 °C-heated NTO (223.9 mAh g^{-1}). Nevertheless, when the 350 and 500 °C heated NTO cells were continuously cycled, their capacities steadily increased. One such cell containing 500 °C-heated NTO is shown in Figure 4a. When using a lower initial discharge cut-off voltage of 0.05 V instead of 0.1 V *vs.* Na^+/Na, the reversible capacities (2nd discharge capacities) increased substantially from 51.7 to 194.2 mAh g^{-1} (Figures 4a & 4b). These observations suggest that NTOs heated at 350 and 500 °C need to be completely 'activated' either by more cycles (discharge steps) or discharge to a lower voltage to assess their whole capacity, similar to what were previously reported for anatase TiO_2 anodes.[24-26] Therefore, to ensure the complete 'activation' of the materials, we employed a cycling protocol including an initial 'activation' cycle for 350, 500 and 800 °C-heated NTO. The discharge cut-off voltage was set at 0.05 V *vs.* Na^+/Na in the initial cycle and then increased to 0.1 V for the subsequent cycles while the charge cut-off voltage was always kept at 2.0 V. Figures S8a and 4c compared respectively their first- and second cycle voltage profiles. The three plateau-like features observed for 60 °C-heated NTO became less visible after vacuum drying at 100 °C, while the 350 °C- and 500 °C heated NTOs showed rather sloping voltage profiles. The material heated at the highest temperature of 800 °C regained some plateau-like features but at somewhat higher potentials, as is also clear in the derivative curves (Figure 4d). Note that the voltage profile of cells containing 800 °C-heated NTO is rather like that obtained for $Na/Na_2Ti_6O_{13}$ cells,[27, 28] providing additional evidence for their structural similarity. The initial Coulombic efficiency (ICE) was found to decrease with the increase of treatment temperature (Figure S8b). Differential electrochemical mass spectrometry (DEMS) results show less H_2 generation during the initial discharge in the cell made with 500 °C-heated NTO (0.09 *u*mol $mg_{active\ material}^{-1}$) than in the cell made with 60 °C-heated NTO (0.13 *u*mol $mg_{active\ material}^{-1}$) (Figure S9). These observations suggest that H_2 generation contributes to the initial

inefficiency, but other factors may also affect ICE such as irreversible reactions involving the electrolytic solution, which are particularly sensitive to the lower cutoff voltage. NTOs heated at 60 (228.1 mAh g^{-1}), 100 (229.8 mAh g^{-1}), 350 (234.6 mAh g^{-1}), and 500 °C (184.0 mAh g^{-1}) delivered higher reversible capacities during the second discharge than NTO heated at 800 °C (82.3 mAh g^{-1}), suggesting that NTOs heated at lower temperatures with layered and/or the unidentified intermediate structure result in higher sodium capacities than NTO heated at higher temperatures with the tunnel structure. The average sodium storage voltage gradually decreased from 0.75 V *vs.* Na^+/Na for the 60 °C-heated NTO to 0.68 V and 0.60 V for 100 °C- and 350 °C heated NTOs and reached the lowest value of 0.58 V for the 500 °C-heated NTO. It then slightly increased to 0.63 V for 800 °C-heated NTO. The average sodium storage voltages were calculated based on $U_{average} = E_{discharge} / Q_{discharge}$, where $E_{discharge}$ and $Q_{discharge}$ refer to energy density and capacity over the full discharge curve. Figure 4e depicts the discharge/charge capacity retention over 50 cycles at the lowest current rate of 8 mA g^{-1} (0.008 mA cm^{-2}). Capacities of 147.9 and 152.7 mAh g^{-1} were obtained at the 50th cycle for 60 °C- and 100 °C heated NTOs, corresponding to 64.8 % and 66.4 % of the second discharge capacity. In contrast, substantially improved capacity retention was achieved for NTOs heated at the moderate temperatures of 350 and 500 °C with higher capacities of 191.6 and 173.5 mAh g^{-1} in the 50th cycle, accounting for 81.7 % and 94.3 % of the second discharge capacity. NTO heated at the highest temperature of 800 °C retained 94.1 % of its reversible capacity at 50th cycle; however, the capacity is relatively low (77.2 mAh g^{-1}). A comparison of the capacity evolution in the high-voltage (1.0 – 2.0 V *vs.* Na^+/Na) and low-voltage (0.1 – 1.0 V *vs.* Na^+/Na) regions revealed that 500 °C-heated NTO exhibits lower capacity and more stable cycling at high

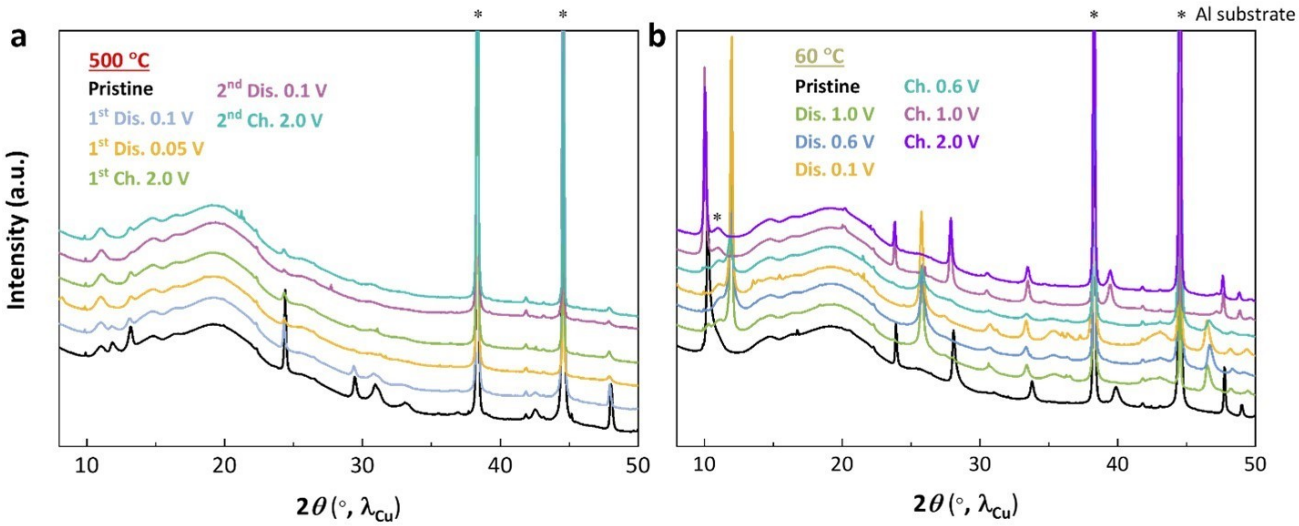

voltages than the 60 °C-heated NTO, whereas less significant differences were observed in the low voltage region (Figure S10). In addition, compared with the 60 °C-heated NTO, the two low-voltage redox peaks located at ça. 0.5 and 0.65 V are less obvious and the high-voltage redox peak at ca. 1.25 V is absent in the cyclic voltammogram for 500 °C-heated NTO (Figure S11). As demonstrated in our previous work,[7] both the high- and low-voltage processes show a hybrid reaction mechanism involving surface reactions and reductive intercalation, and the high-voltage processes are the main contributors to the capacity fading. The reduced gas generation could also contribute to the improved cycling stability of 500 °C-heated NTO. As monitored by DEMS, higher amount of H_2 (0.10 *u*mol $mg_{active\ material}^{-1}$) evolves in the 2nd cycle from the cell made with 60 °C-heated NTO than the cell made with 500 °C-heated NTO (0.05 *u*mol $mg_{active\ material}^{-1}$). To further assess the cycling performance of 500 °C-heated NTO, cells were cycled at elevated current rates after employing the initial 'activation' cycle (Figure S12). The results show that 80.1 % of the reversible capacity (150.8 mAh g^{-1}) was retained in the 743th cycle at a current rate of 200 mA g^{-1} and 90.9 % of the reversible capacity (137 mAh g^{-1}) was obtained in the 549th cycle at a current rate of 500 mA g^{-1}.

Figure 5. *Ex situ* synchrotron XRD patterns of (a) 500 °C- and (b) 60 °C heated NTOs as a function of depth of discharge and charge.

Next, galvanostatic intermittent titration technique (GITT) measurements were carried out in the first discharge to study the initial 'activation' process of 500 °C-heated NTO (Figure 4f). The reduced polarization observed at the higher depth of discharge indicates improvement of electrode kinetics. This observation is consistent with the electrochemical impedance spectroscopy (EIS) result (inset in Figure 4f) showing a continuous decrease in the cell impedance during discharge. To investigate the cycling-induced structural evolutions of 500 °C-heated NTO, *ex situ* synchrotron XRD experiments were performed on electrodes cycled to selected states of discharge and charge (Figure 5a). A continuous decrease in the XRD peak intensity were observed during the initial discharge, indicating that the pristine material gradually transformed into an amorphous phase. Most reflections vanished at the end of the initial discharge (0.05 V *vs.* Na^+/Na) and remained nearly unchanged upon subsequent cycling, indicating that this amorphozation was irreversible and occurred only during the initial sodiation, especially within the voltage range between 0.1 and 0.05 V *vs.* Na^+/Na. The newly formed amorphous phase was electrochemically active and contributed to the subsequent sodium ion storage. The formation of an amorphous phase from the shell to the core of 500°C-heated NTO particles was also evident from *ex situ* high-resolution transmission electron microscope (HRTEM) images (Figure S13). Note that some residual crystalline fringes were seen at the end of discharge due to the incomplete sodiation. Overall, the XRD results agreed well with the shape changes of the voltage profiles (Figure 4b). The long plateau between 0.1 and 0.05 V *vs.* Na^+/Na in the initial discharge is related to the formation of the amorphous phase. It converted into a sloping voltage profile during the subsequent charge and maintained its sloping shape for the subsequent cycles. On the other hand, for the 60 °C-heated NTO, which does not exhibit the initial 'activation' behavior nor the voltage profile shape change, the structural evolution was found to be largely reversible in the initial cycle (Figure 5b). Note that, unlike the anhydrous *Cmcm* structure obtained for NTO powder that was vacuum dried at 60 °C (Figure S4a), the pristine 60 °C-heated NTO electrode remains a partially hydrated *Immm* structure showing a broad (020) reflection at ca. 2θ = 10.2° (Figure 5b). This discrepancy could be explained by their different initial water content, *i.e.*, the NTO electrode took up additional water during the water-based electrode preparation. On discharging to 1.0 V *vs.* Na^+/Na and below, the (020) reflection line moved to higher angles. Simultaneously, the two reflection lines at 2θ = 23.9° and 28.0° merged into one single peak at 2θ = 25.8° and new broad diffraction peaks

appeared at 2θ = 35.3° and 43.1°, This structural change may also contribute to the cycling instability of 60 °C-heated NTO at higher voltages. Figure S14 shows the new broad peaks in the synchrotron XRD pattern of the electrode discharged to 0.6 V, but it is difficult to assign these to a

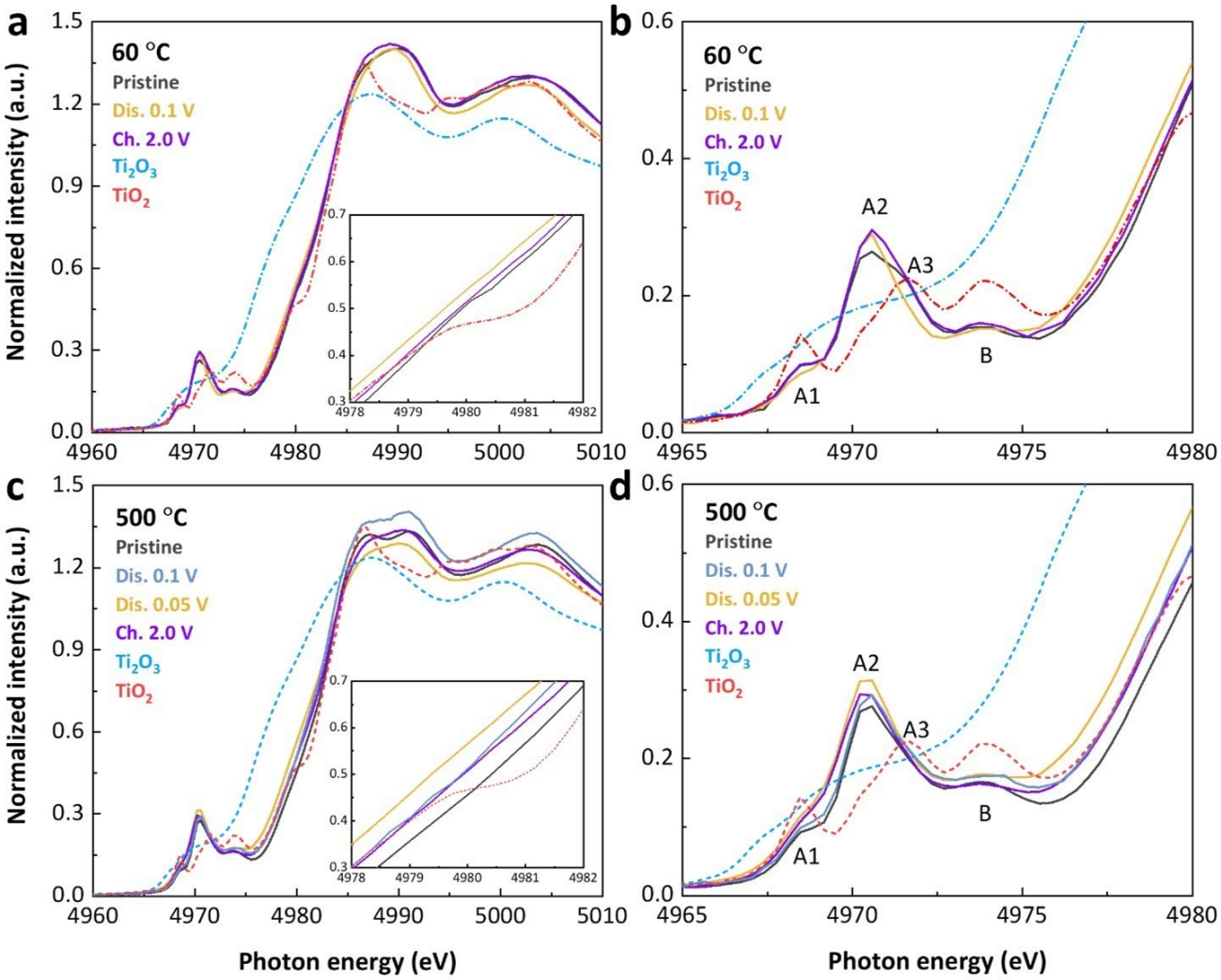

structure. An earlier report on a similar system, however, showed evidence that the high-voltage plateau at ca. 1.25 V is associated with the co-existence of two phases; one that is C-type and another that has a triclinic lattice.[11] The (020) reflection line moves sharply to the right for the sodiated material, suggesting that residual water in the pristine electrode was expelled upon the insertion of sodium ions, leading to the formation of a dehydrated structure. Further desodiation to 1.0 V *vs.* Na^+/Na and above resulted in a structure like the pristine phase with the (020) reflection positioned at a slightly lower angle than that of the pristine one, most probably due to the co-intercalation of adventitious water or solvent molecules from the electrolyte solution. Such water/solvent co-intercalation behavior has previously been reported for another lepidocrocite-type sodium titanate anode.[10]

Figure 6. Ti K-edge X-ray absorption near-edge structure (XANES) spectra of (a) 60 °C- and (c) 500 °C-heated NTO as a function of depth of discharge and charge during the initial electrochemical cycle. Insets in (a) and (c) show the zoom-in of the edge region. (b) and (d) show the zoom-in of the pre-edge region.

The reaction mechanisms of 60 and 500 °C-heated NTOs were then investigated by X-ray absorption spectroscopy (XAS) at the Ti K-edge. For both materials, the absorption edge gradually shifted toward lower excitation energies on discharge and back to higher energies on charge (Figures 6 & S15), confirming that the reduction and oxidation of titanium compensated for the charge passed during their sodiation and desodiation. The pre-edge intensities of O-K XAS spectra are known to be strongly dependent on the hybridization strength between orbitals of oxygen and transition metals, and can represent changes in the oxidation state of transition metals.[29] As shown in Figure S16, the O-K pre-edge intensity of NTOs progressively decrease during discharge and increase during charge, indicating a lower titanium oxidation state in the discharged states and a higher titanium oxidation state in the charged states, which is consistent with the Ti K-edge XAS results. Additional evidence of titanium reduction was provided by optical images of the discharged carbon-free NTO electrodes showing a color-change from white to dark blue, characteristic of trivalent titanium (Figure S17). Linear combination fitting of the Ti K-edge XANES spectra using Ti_2O_3 and TiO_2 references estimated 13.1 % and 22.9 % of Ti^{4+} reduction to Ti^{3+} respectively for 60 °C- and 500 °C-heated NTOs. However, on the assumption that all the experimentally obtained reversible sodium capacities are due to reductive intercalation, 78.7 % and 63.5 % of Ti^{4+} should be reduced to Ti^{3+} in 60 °C- and 500 °C-heated NTOs at their end of discharge states. This discrepancy suggests that a hybrid reaction mechanism involving both reductive intercalation and surface reactions is responsible for the large capacities of NTOs heated at 60 and 500 °C, in accordance with our previous findings based on electrochemical analyses.[7] Noteworthy, XANES results reveal more Ti^{4+} reduction in the 500 °C-heated NTO than in the 60 °C-

heated NTO after discharge despite of slightly lower capaicty for the former, which somewhat in line with previous cycling data showing reduced surface-related capacities at high voltages (1.0 - 2.0 V *vs.* Na^+/Na) due to modified surface chemistry by heat treatment at 500 °C.

Conclusion

In this work, we studied in detail the structural changes and electrochemical properties of lepidocrocite-type sodium titanate $Na_{0.74}Ti_{1.815}\bullet_{0.185}O_4\bullet 1.27H_2O$ (NTO) under different post-synthesis heating conditions. *In situ* synchrotron high-temperature XRD and *ex situ* Raman spectroscopy showed that the layered hydrous *Immm* structure of NTO first converts to a layered anhydrous *Cmcm* structure at 200 °C, and eventually transforms to a $Na_2Ti_6O_{13}$-like tunnel structure at 700 °C *via* an unidentified intermediate phase. Electrochemical characterization revealed that NTOs heated at lower temperatures with layered structures generally exhibit higher capacities than NTOs heated at high temperature with tunnel structure. The voltage profiles also change as a function of heating temperature, with the materials prepared at higher temperatures exhibiting less high voltage (1.0 - 2.0 V *vs.* Na^+/Na) capacities than those prepared at lower temperatures. This is significant because the high voltage processes are primarily associated with surface reactions that result in severe capacity fading. The material heated at 500 °C could retain 94.3% of its capacity of 184 mAh g^{-1} over 50 cycles at a moderate rate. This material also required an 'activation' process involving amorphization; either by an initial cycle to 0.05 V *vs.* Na^+/Na or prolonged cycling, to reach its full capacity. In contrast, NTO heated at low temperatures (*e.g.*, 60 °C) remains crystalline and undergoes reversible phase change with a large reversible capacity of 228 mAh g^{-1} but retains only 64.8 % of its capacity over 50 cycles. NTO heated at 800 °C delivers a low capacity of 82.3 mAh g^{-1} although the capacity retention is 94.1 % over 50 cycles. Synchrotron X-ray absorption spectroscopy implied that the relatively large capacities obtained for 60 °C- and 500 °C-heated NTOs were due to both reductive intercalation and surface reactions.

Author contributions

M. Doeff conceived and supervised the project. W. Yin designed the experiments, conducted the electrochemical, XRD, XANES experiments and analyzed the data. G. Barim performed the FTIR and Raman measurements. X. Peng performed the TEM experiments. X. Peng and M. C. Scott analyzed the TEM results. E. Kedzie conducted the DEMS measurements. E. Kedzie and B. D. McCloskey analyzed the DEMS data. W. Yin wrote the manuscript with contributions from all authors.

Acknowledgements

This work was supported by the Assistant Secretary for Energy, Efficiency and Renewable Energy, Office of Vehicle Technologies of the U.S. Department of Energy under Contract No. DE-AC02-05CH11231. Work at the Molecular Foundry of Lawrence Berkeley National Lab (LBNL) was supported by the Office of Science, Office of Basic Energy Sciences of the U.S. Department of Energy under Contract No. DE-AC02-05CH11231. We would like to acknowledge the use of the Stanford Synchrotron Radiation Lightsource (SSRL), SLAC National Accelerator Laboratory, that is supported by the U.S. Department of Energy, Office of Science, Office of Basic Energy Sciences under Contract No. DE-AC02-76SF00515. This document was prepared as an account of work sponsored by the United States Government. While this document is believed to contain correct information, neither the United States Government nor any agency thereof, nor the Regents of the University of California, nor any of their employees, makes any warranty, express or implied, or assumes any legal responsibility for the accuracy, completeness, or usefulness of any information, apparatus, product, or process disclosed, or represents that its use would not infringe privately owned rights. Reference herein to any specific commercial product, process, or service by its trade name, trademark, manufacturer, or otherwise, does not necessarily constitute or imply its endorsement, recommendation, or favoring by the United States Government or any agency thereof, or the Regents of the University of California. The views and opinions of authors expressed herein do not necessarily state or reflect those of the United States Government or any agency thereof or the Regents of the University of California. We thank Dr Sami Sainio, Dr Sang-Jun Lee, and Dr Dennis Nordlund for collecting soft X-ray absorption spectra. We would also like to thank Dr Charles Troxel Jr, Dr Nicholas A. Strange, Dr Erik J. Nelson, and Dr Matthew J. Latimer for their support at SSRL.

Conflict of interest

There are no conflicts of interest to declare.

Table of Contents

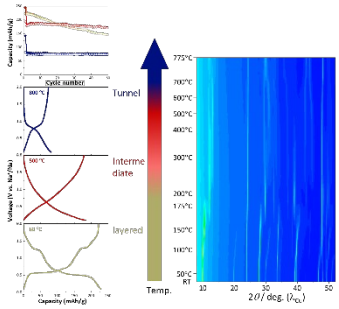

A simple post-synthesis heating approach tailors the crystal structure, surface chemistry, and electrochemical properties of sodium titanate anode.

Keywords: Sodium-ion batteries • Anode materials • Sodium titanate • Post-synthesis heating

References

1. P. Greim, A. A. Solomon and C. Breyer, *Nat Commun*, 2020, **11**, 4570.
2. K. M. Abraham, *ACS Energy Letters*, 2020, DOI: 10.1021/acsenergylett.0c02181, 3544-3547.
3. J.-M. Tarascon, *Joule*, 2020, **4**, 1616-1620.
4. N. Tapia-Ruiz, A. R. Armstrong, H. Alptekin, M. A. Amores, H. Au, J. Barker, R. Boston, W. R. Brant, J. M. Brittain, Y. Chen, M. Chhowalla, Y.-S. Choi, S. I. R. Costa, M. Crespo Ribadeneyra, S. A. Cussen, E. J. Cussen, W. I. F. David, A. V. Desai, S. A. M. Dickson, E. I. Eweka, J. D. Forero-Saboya, C. P. Grey, J. M. Griffin, P. Gross, X. Hua, J. T. S. Irvine, P. Johansson, M. O. Jones, M. Karlsmo, E. Kendrick, E. Kim, O. V. Kolosov, Z. Li, S. F. L. Mertens, R. Mogensen, L. Monconduit, R. E. Morris, A. J. Naylor, S. Nikman, C. A. O'Keefe, D. M. C. Ould, R. G. Palgrave, P. Poizot, A. Ponrouch, S. Renault, E. M. Reynolds, A. Rudola, R. Sayers, D. O. Scanlon, S. Sen, V. R. Seymour, B. Silván, M. T. Sougrati, L. Stievano, G. S. Stone, C. I. Thomas, M.-M. Titirici, J. Tong, T. J. Wood, D. S. Wright and R. Younesi, *Journal of Physics: Energy*, 2021, **3**.
5. A. Rudola, A. J. R. Rennie, R. Heap, S. S. Meysami, A. Lowbridge, F. Mazzali, R. Sayers, C. J. Wright and J. Barker, *Journal of Materials Chemistry A*, 2021, **9**, 8279-8302.
6. I. M. Markus, S. Engelke, M. Shirpour, M. Asta and M. Doeff, *Chemistry of Materials*, 2016, **28**, 4284-4291.
7. W. Yin, J. Alvarado, G. Barim, M. C. Scott, X. Peng and M. M. Doeff, *MRS Energy & Sustainability*, 2021, DOI: 10.1557/s43581-021-00008-6.
8. J. Alvarado, G. Barim, C. D. Quilty, E. Yi, K. J. Takeuchi, E. S. Takeuchi, A. C. Marschilok and M. M. Doeff, *Journal of Materials Chemistry A*, 2020, **8**, 19917-19926.
9. M. Shirpour, J. Cabana and M. Doeff, *Energy & Environmental Science*, 2013, **6**.
10. M. Shirpour, J. Cabana and M. Doeff, *Chemistry of Materials*, 2014, **26**, 2502-2512.
11. A. Katogi, K. Kubota, K. Chihara, K. Miyamoto, T. Hasegawa and S. Komaba, *ACS Applied Energy Materials*, 2018, **1**, 3630-3635.
12. T. Maluangnont, N. Chanlek, T. Suksawad, N. Tonket, P. Saikhamdee, U. Sukkha and N. Vittayakorn, *Dalton Trans*, 2017, **46**, 14277-14285.
13. T. Charoonsuk, S. Sriphan, P. Pulphol, W. Vittayakorn, N. Vittayakorn and T. Maluangnont, *Inorg Chem*, 2020, DOI: 10.1021/acs.inorgchem.0c02264.
14. Y. Su and M. L. Balmer, *J. Phys. Chem. B*, 2000, **104**, 8160-8169.
15. T. Gao, H. Fjellvåg and P. Norby, *J. Phys. Chem. B* 2008, **112**, 9400–9405.
16. S.-H. Byeon, S.-O. Lee and H. Kim, *Journal of Solid State Chemistry*, 1997, **130**, 110-116.
17. C.-W. Peng, M. Richard-Plouet, T.-Y. Ke, C.-Y. Lee, H.-T. Chiu, C. Marhic, E. Puzenat, F. Lemoigno and L. Brohan, *Chem. Mater.* , 2008, **20**, 7228–7236.
18. C. E. BAMBERGER and G. M. BEGUN, *J. Am. Ceram. SOC*, 1987, **70**, C-48-C-51.
19. N. Jiang, D. Su and J. C. H. Spence, *Physical Review B*, 2007, **76**.
20. R. Ma, K. Fukuda, T. Sasaki, M. Osada and Y. Bando, *J. Phys. Chem. B* 2005, **109**, 6210-6214.
21. J. Guo, *International Journal of Quantum Chemistry*, 2009, **109**, 2714-2721.
22. C. Bittencourt, P. Kruger, M. J. Lagos, X. Ke, G. Van Tendeloo, C. Ewels, P. Umek and P. Guttmann, *Beilstein J Nanotechnol*, 2012, **3**, 789-797.
23. P. Krüger, *Physical Review B*, 2010, **81**.
24. L. Wu, D. Bresser, D. Buchholz, G. A. Giffin, C. R. Castro, A. Ochel and S. Passerini, *Advanced Energy Materials*, 2015, **5**.
25. L. Wu, D. Buchholz, D. Bresser, L. Gomes Chagas and S. Passerini, *Journal of Power Sources*, 2014, **251**, 379-385.
26. L. Ling, Y. Bai, Y. Li, Q. Ni, Z. Wang, F. Wu and C. Wu, *ACS Appl Mater Interfaces*, 2017, **9**, 39432-39440.
27. M. M. Doeff, J. Cabana and M. Shirpour, *Journal of Inorganic and Organometallic Polymers and Materials*, 2013, **24**, 5-14.
28. C. Wu, Z. G. Wu, X. Zhang, R. Rajagopalan, B. Zhong, W. Xiang, M. Chen, H. Li, T. Chen, E. Wang, Z. Yang and X. Guo, *ACS Appl Mater Interfaces*, 2017, **9**, 43596-43602.

29. S. Roychoudhury, R. Qiao, Z. Zhuo, Q. Li, Y. Lyu, J. H. Kim, J. Liu, E. Lee, B. J. Polzin, J. Guo, S. Yan, Y. Hu, H. Li, D. Prendergast and W. Yang, *Energy & Environmental Materials*, 2020, **4**, 246-254.